



Cite this: *RSC Adv.*, 2025, 15, 9985

# $\text{Ti}_3\text{C}_2/\text{CuWO}_4/\text{Pt}$ nanozyme: photothermal-enhanced chemodynamic antibacterial effects induced by NIR†

Simin Yuan,<sup>a</sup> Lianyuan Ge,<sup>b</sup> Yi Li,<sup>b</sup> Xiaohong Wang,<sup>b</sup> Zhongyuan Liu,<sup>a</sup> Yang Cao <sup>\*b</sup> and Linglin Yang<sup>\*ac</sup>

With the growing issue of antibiotic resistance, it has become increasingly crucial to develop highly efficient antimicrobial materials. While the single-component nanozyme systems exhibited some catalytic activity, their efficiency remains suboptimal. This study presents a  $\text{Ti}_3\text{C}_2/\text{CuWO}_4/\text{Pt}$  hybrid nanozyme composed of photothermal agents and nanozymes, which leverages the photothermal effect to enhance nanozyme activity and achieve efficient antimicrobial effects. The composite material exhibited peroxidase (POD)-like catalytic activity, effectively converting hydrogen peroxide ( $\text{H}_2\text{O}_2$ ) into hydroxyl radicals ( $\cdot\text{OH}$ ). Meanwhile, the  $\text{Ti}_3\text{C}_2/\text{CuWO}_4/\text{Pt}$  material demonstrated high photothermal conversion ability, which not only promoted the generation of  $\cdot\text{OH}$  under near-infrared (NIR) light irradiation, but also facilitated copper ( $\text{Cu}^{2+}$ ) ions release from the  $\text{CuWO}_4$  nanozyme, thereby further augmenting its catalytic activity. After 4 to 5 min of light irradiation, the  $\text{Ti}_3\text{C}_2/\text{CuWO}_4/\text{Pt}$  nanozyme exhibited significant antimicrobial performance against both *Escherichia coli* (*E. coli*) and *Staphylococcus aureus* (*S. aureus*). In summary, this work presents a  $\text{Ti}_3\text{C}_2/\text{CuWO}_4/\text{Pt}$  nanoplatfrom that utilizes the photothermal effect to enhance the chemodynamic antimicrobial activity, showcasing its potential applications in antibiotic-free antimicrobial fields.

Received 16th December 2024  
Accepted 20th March 2025

DOI: 10.1039/d4ra08791g

rsc.li/rsc-advances

## 1 Introduction

Bacterial infections pose a significant threat to public health worldwide.<sup>1,2</sup> Antibiotics are commonly utilized to treat bacterial infections, though the excessive use of broad-spectrum antibiotics has hastened the rise of resistant microbes.<sup>3,4</sup> Due to the emergence of superbugs, the therapeutic efficacy of antibiotics has significantly declined, thereby posing a substantial challenge to the current treatment system.<sup>5</sup> In this context, the development of new antimicrobial agents to replace antibiotics is urgently needed.

Nanomaterials demonstrate significant potential in treating bacterial infections because of their broad-spectrum antimicrobial properties, resistance to drug resistance, along with minimal biotoxicity.<sup>6</sup> Photothermal therapy (PTT) based on nanomaterials has attracted widespread attention for its minimally invasive nature, high efficiency, and deep tissue penetration.<sup>7</sup> During PTT, photothermal nanomaterials absorb light

energy and transform it into localized heat when exposed to a near-infrared (NIR) laser, leading to bacterial cell death.<sup>8</sup> In recent years, two-dimensional (2D)  $\text{Ti}_3\text{C}_2$  MXene materials, known for their adjustable physicochemical characteristics, excellent biocompatibility, and high photothermal conversion efficiency, have gained significant attention in photothermal anti-tumour and antimicrobial therapies.<sup>9,10</sup> Wu *et al.* investigated the antimicrobial efficacy of MXene in PTT, demonstrating that  $\text{Ti}_3\text{C}_2$  MXene exhibited significant bacteriostatic effects against *Escherichia coli* (*E. coli*) and *Staphylococcus aureus* (*S. aureus*) following 20 min of NIR light irradiation.<sup>11</sup> However, extended high-intensity laser exposure may adversely affect normal cells and tissues, necessitating the development of materials that function effectively at lower power and shorter exposure durations.

Chemodynamic therapy (CDT), in contrast, involves the catalytic process of peroxidase-like (POD) nanomaterials or Fenton-like reactions to transform endogenous hydrogen peroxide ( $\text{H}_2\text{O}_2$ ) into highly reactive hydroxyl radicals ( $\cdot\text{OH}$ ), resulting in irreversible oxidative damage to bacterial DNA, proteins, as well as other cellular components.<sup>12</sup> Various POD-like nanomaterials (nanozymes) containing transition metal or noble metal cores, such as Cu, Fe, Mn, and Pt, have been designed and applied in CDT for bacterial infection treatment.<sup>13–15</sup> For instance, Cui *et al.* synthesized a  $\text{CuWO}_4$  nanozyme characterized by small size, high stability, and

<sup>a</sup>College of Chemical Engineering Sichuan University of Science & Engineering, Zigong 643000, P. R. China. E-mail: yanglinglin2003@163.com

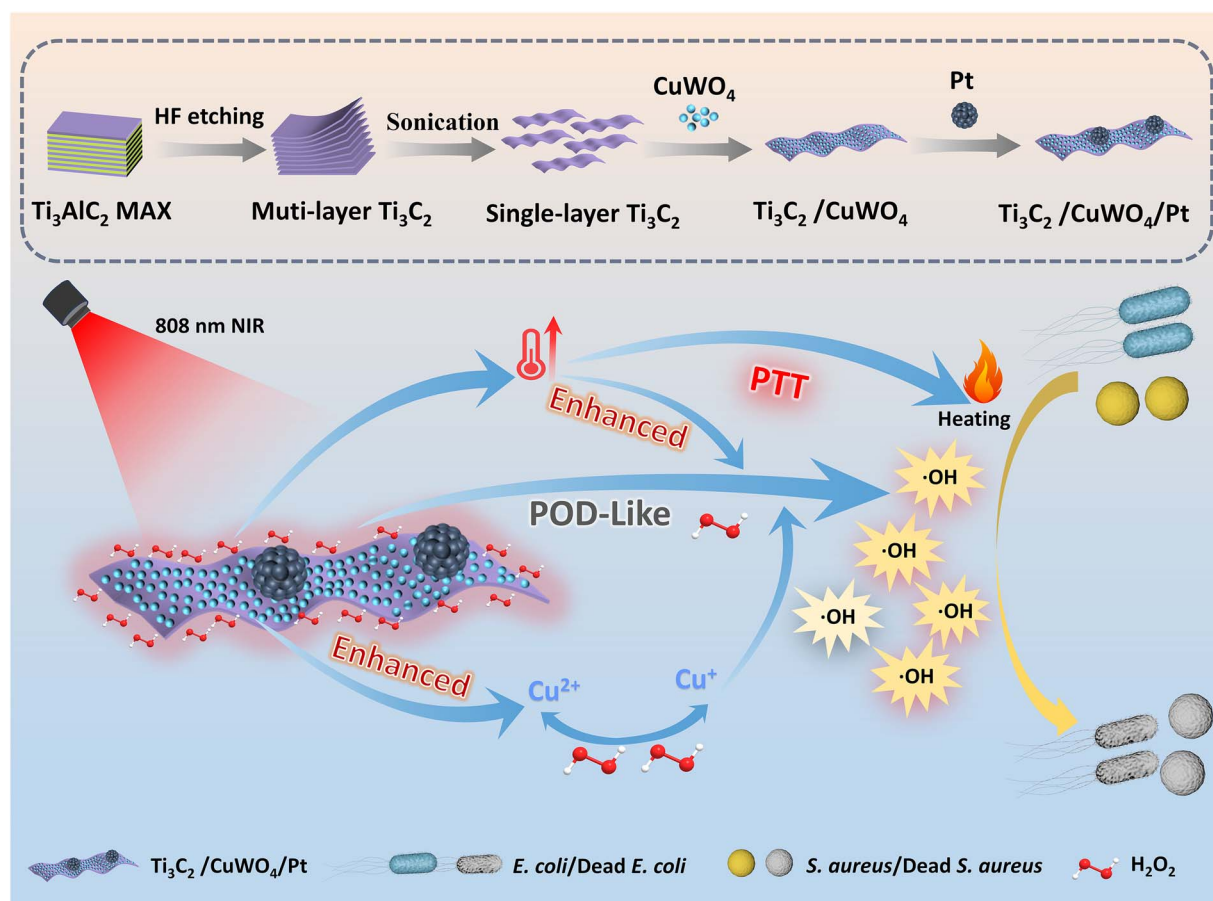
<sup>b</sup>State Key Laboratory of Marine Resource Utilization in the South China Sea, Hainan University, Haikou 570228, P. R. China. E-mail: cy507@hainanu.edu.cn

<sup>c</sup>Shenjiu Group Co., Ltd, Luzhou 646000, P. R. China

† Electronic supplementary information (ESI) available. See DOI: <https://doi.org/10.1039/d4ra08791g>


responsiveness to NIR light, which exhibits POD-like activity *via* Fenton-like reactions, enhancing bacterial cell death when combined with photodynamic therapy (PDT).<sup>16</sup> However, the limited efficiency of nanozymes in catalysis significantly constrains their application in the antimicrobial field.<sup>17</sup> Researchers have integrated photothermal materials into nanozyme systems to promote enzyme activity through elevated temperatures.<sup>18</sup> For instance, a metal-organic framework loaded with Pt nanoparticles (Au NR@H-ZIF-8@Pt) exhibits favourable photothermal properties under NIR irradiation, with a photothermal conversion efficiency of 31.9%.<sup>19</sup> Additionally, it demonstrates high peroxidase-like activity, which contributes to broad-spectrum antibacterial effects. Another study has demonstrated that  $\text{Cu}_x\text{O}@PDA$  nanozymes not only exhibit a relatively high photothermal conversion efficiency (39.8%) but also enhance peroxidase-like activity under NIR irradiation.<sup>20</sup> Nevertheless, the photothermal effect's impact on single-component nanozyme activity enhancement has proven limited.<sup>21</sup> Therefore, an effective and rapid strategy is required to enhance nanozyme activity to achieve synergistic antimicrobial effects through photothermal enhancement of chemodynamics.

In this work,  $\text{CuWO}_4$  and Pt nanozymes were incorporated into the  $\text{Ti}_3\text{C}_2$  photothermal system to develop a hybrid nanozyme composed of photothermal agents and nanozymes. This system not only achieves superior photothermal conversion efficiency but also enables synergistic antibacterial treatment by enhancing nanozyme activity through photothermal effects (Scheme 1). Initially, ultra-thin  $\text{Ti}_3\text{C}_2$  nanosheets were prepared, followed by anchoring  $\text{CuWO}_4$  nanoparticles onto the nanosheet surface *via* physical adsorption and adding Pt nanozymes, resulting in a stable  $\text{Ti}_3\text{C}_2/\text{CuWO}_4/\text{Pt}$  composite structure. The photothermal effect of  $\text{Ti}_3\text{C}_2$  facilitated hydroxyl radical generation, thereby enhancing the catalytic activity of the  $\text{CuWO}_4$  and Pt nanozymes. Furthermore, this hybrid nanozyme composed of photothermal agents and nanozymes structure effectively compensated for the limitations of a single-component nanozyme, remarkably improving catalytic activity under photothermal assistance. The prepared  $\text{Ti}_3\text{C}_2/\text{CuWO}_4/\text{Pt}$  material demonstrated a photothermal efficiency of 66%. Additionally, this material exhibited significant antimicrobial effects against common pathogenic bacteria *E. coli* and *S. aureus* within 4 to 5 min of NIR light irradiation. Based on current findings, we believe that the  $\text{Ti}_3\text{C}_2/\text{CuWO}_4/\text{Pt}$  composite material shows considerable potential for antimicrobial applications.



**Scheme 1** Schematic diagram of the preparation process of  $\text{Ti}_3\text{C}_2/\text{CuWO}_4/\text{Pt}$  composites and photothermal enhancement of the antimicrobial properties of nanozymes.



## 2 Experimental

### 2.1 Materials and methods

Ti<sub>3</sub>AlC<sub>2</sub> was purchased from Foshan Xinxi Technology Co., Ltd. Hydrofluoric acid (HF), lithium chloride anhydrous (LiCl), copper chloride dihydrate (CuCl<sub>2</sub>·2H<sub>2</sub>O), sodium tungstate dihydrate (Na<sub>2</sub>WO<sub>4</sub>·2H<sub>2</sub>O), and 3,3',5,5'-tetramethylbenzidine (TMB) were bought from Shanghai Macklin Biochemical Co., Ltd. Chloroplatinic acid hexahydrate (H<sub>2</sub>PtCl<sub>6</sub>·6H<sub>2</sub>O) was acquired from Shanghai Aladdin Biochemical Technology Co., Ltd. Trisodium citrate dihydrate (C<sub>6</sub>H<sub>5</sub>Na<sub>3</sub>O<sub>7</sub>·2H<sub>2</sub>O) was obtained from Guangdong Guanghua Sci-Tech Co., Ltd. Hydrochloric acid (HCl) and hydrogen peroxide 30% (H<sub>2</sub>O<sub>2</sub>) were procured from Xilong Scientific Co., Ltd. Acetic acid (CH<sub>3</sub>-COOH), sodium acetate trihydrate (CH<sub>3</sub>COONa·3H<sub>2</sub>O), and sodium chloride (NaCl) were purchased from Guangzhou Chemical Reagent Factory. Bacterial strains *E. coli* (CMCC (B) 44102) and *S. aureus* (CMCC (B) 26003) were obtained from Shanghai Luwei Technology Co., Ltd. Tryptone, Yeast Extract, and Agar were acquired from Sangon Biotech (Shanghai) Co., Ltd. Live & Dead Bacterial Staining Kit was purchased from Yeasen Biotechnology (Shanghai) Co., Ltd. Ethyl alcohol was bought from Sinopharm Chemical Reagent Co., Ltd. Glutaraldehyde fixed solution was procured from Phygene Biotechnology Co., Ltd.

### 2.2 Preparation of Ti<sub>3</sub>C<sub>2</sub> nanosheets

Ti<sub>3</sub>C<sub>2</sub> nanosheets were synthesized by adapting previously reported methods.<sup>22</sup> 20 mL 49% HF and 20 mL HCl (12 M) were combined with 10 mL of deionized water and stirred for 10 min. Then 2.0 g of Ti<sub>3</sub>AlC<sub>2</sub> powder was gradually added in portions, and the reaction proceeded for 12 h at 35 °C. The mixture was then centrifuged at 3500 rpm for 2 min, repeated six times to remove residual acids and impurities. Separately, 2 g of LiCl was dissolved in 40 mL of deionized water. The precipitate collected by centrifugation was dispersed into the prepared solution and stirred at ambient temperature for 12 h. The supernatant was collected after two times of centrifugation (3500 rpm, 2 min), followed by ultrasonicated under an argon environment for 15 min. Finally, the supernatant was taken through centrifugation at 4000 rpm for 30 min and freeze-dried.

### 2.3 Preparation of CuWO<sub>4</sub> and Pt

CuWO<sub>4</sub> nanodots were synthesized following the procedure reported in previous studies.<sup>16,23</sup> Firstly, 8 mL of CuCl<sub>2</sub>·2H<sub>2</sub>O (0.5 M) was combined with 10 mL of Na<sub>2</sub>WO<sub>4</sub>·2H<sub>2</sub>O (0.4 M). After stirring for 30 min, 16 mL of sodium citrate (0.5 M) was added to the mixture. Following 1 h of stirring, the mixture was placed into an autoclave and underwent hydrothermal treatment in an oven at 180 °C for 12 h. After cooling to ambient temperature, the supernatant was separated through centrifugation and dialyzed in deionized water for 24 h. Finally, the CuWO<sub>4</sub> nanodots were freeze-dried for further use.

Pt nanozymes were prepared by sodium citrate reduction.<sup>24,25</sup> Briefly, 20 mL of chloroplatinic acid hexahydrate (0.02 M) was mixed with 16 mL of sodium citrate (0.5 M) and stirred for

30 min. This mixture was then transferred to an autoclave tank and hydrothermally heated in an oven at 180 °C for 12 h. After cooling to room temperature, the precipitate was collected by centrifugation at 12 000 rpm for 1 min. Finally, the precipitate was dispersed in 20 mL of deionized water for use.

### 2.4 Preparation of Ti<sub>3</sub>C<sub>2</sub>/CuWO<sub>4</sub>/Pt

10 mL of 1 mg mL<sup>-1</sup> CuWO<sub>4</sub> was combined with 10 mL of 2 mg mL<sup>-1</sup> Ti<sub>3</sub>C<sub>2</sub>, stirring continuously at room temperature. After thorough mixing, 10 mL of Pt was introduced into the mixture, followed by vigorous stirring for 4 h. The Ti<sub>3</sub>C<sub>2</sub>/CuWO<sub>4</sub>/Pt composite was washed three times with deionized water to eliminate unreacted reagents and impurities.

Ti<sub>3</sub>C<sub>2</sub>/CuWO<sub>4</sub> was prepared without Pt in the appeal step and Ti<sub>3</sub>C<sub>2</sub>/Pt without CuWO<sub>4</sub>.

### 2.5 Characterization

Transmission electron microscopy (TEM, FEI-Tecna G2 F20/F30, USA) was employed to analyse the surface morphology, lattice structure, and elemental composition. Infrared spectroscopy (FTIR, BRUKER TENSOR 27, Germany) was utilized to examine the valence bond composition of the synthesized materials. To investigate the structure and composition of the products, X-ray diffraction (XRD, Smart Lab SE, Japan) and X-ray photoelectron spectroscopy (XPS, Thermo ESCALAB 250XI, USA) were employed. The UV-vis-NIR absorption spectra were recorded using an L5 spectrophotometer (INESA, China). Laser irradiation experiments were performed using a VCL-808 nm NIR laser (Beijing Honglan Photoelectric Technology Co., Ltd, China). The thermal image was captured by a FLIR E6390 thermal imaging camera (FLIR, Estonia). The copper (Cu<sup>2+</sup>) ion content was determined using an inductively coupled plasma optical emission spectrometer (ICP-OES, iCAP PRO, USA). The ability of the material to produce ·OH under radiation was assessed through electron spin resonance (ESR, JES FA200, JEOL). Fluorescence images of bacteria were obtained by MF41 fluorescence microscopy (Guangzhou Mshot Photoelectric Technology Co., Ltd, China). Morphological characteristics of microorganisms were observed using scanning electron microscopy (SEM, Verios G4 UC).

### 2.6 Photothermal experiments

The prepared solution was exposed to NIR laser irradiation, with its temperature change monitored using a thermal infrared imager, according to which the photothermal performance was evaluated. Specifically, 1 mL suspension was irradiated with the NIR laser for 10 min, with the temperature recorded every 30 seconds. Different materials (Ti<sub>3</sub>C<sub>2</sub>/CuWO<sub>4</sub>, Ti<sub>3</sub>C<sub>2</sub>/Pt, Ti<sub>3</sub>C<sub>2</sub>/CuWO<sub>4</sub>/Pt), powers (0.49, 1.09, 1.54, and 2.01 W cm<sup>-2</sup>), and material concentrations (25, 50, 100, and 200 µg mL<sup>-1</sup>) were utilized for this evaluation. In addition, photothermal cycling experiments were performed to assess the photothermal stability of Ti<sub>3</sub>C<sub>2</sub>/CuWO<sub>4</sub>/Pt, with the temperature recorded every 30 seconds. Each cycle consisted of 10 min of irradiation heating and 10 min of natural cooling. Based on the cooling phase, the photothermal conversion efficiency (η) of the composite was calculated using the equation.<sup>26–29</sup>





$$\eta = \frac{hs(T_{\max} - T_{\text{surr}}) - Q_{\text{dis}}}{I(1 - 10^{-A_{808}})}$$

where  $h$  represents the heat transfer coefficient, and  $s$  denotes the surface area of the container.  $T_{\max}$  is the maximum stable temperature reached during the heating process, while  $T_{\text{surr}}$  represents the ambient temperature.  $Q_{\text{dis}}$  corresponds to the dissipated heat,  $I$  denotes the laser power, and  $A$  refers to the absorbance of the composite material at a wavelength of 808 nm.

## 2.7 Analysis of released $\text{Cu}^{2+}$ ions

1 mg  $\text{mL}^{-1}$  suspension of  $\text{Ti}_3\text{C}_2/\text{CuWO}_4/\text{Pt}$  was transferred to a dialysis bag following 5 min of NIR light treatment and without NIR light treatment, respectively. After 12 h of dialysis, the solution outside the dialysis bag was collected, and the changes in  $\text{Cu}^{2+}$  ion concentrations before and after NIR light exposure were analysed using ICP-OES.<sup>30</sup>

## 2.8 Peroxidase-like property

The POD-like activity of  $\text{Ti}_3\text{C}_2/\text{CuWO}_4/\text{Pt}$  nanocomposites was investigated using TMB as substrate. In the experiment, 200  $\mu\text{L}$  of  $\text{Ti}_3\text{C}_2/\text{CuWO}_4/\text{Pt}$  (1 mg  $\text{mL}^{-1}$ ) was added to 1 mL of NaAc-HAc buffer solution. Then 1 mL of TMB (4 mM) and  $\text{H}_2\text{O}_2$  (0.2, 0.4, 0.6, 0.8, 1 mM) were added to the above solution. After illumination for 2 min, the UV-vis absorption spectrum of oxTMB with a characteristic absorption peak at 652 nm was recorded. A control group without illumination was also recorded. Line-weaver-Burk plots were applied to determine the Michaelis-Menten constant ( $K_m$ ) and maximum reaction velocity ( $V_{\max}$ ).<sup>31–33</sup>

$$\frac{1}{v_0} = \frac{K_m}{V_{\max}} \times \frac{1}{[S]} + \frac{1}{V_{\max}}$$

where  $v_0$  is the initial reaction rate.  $[S]$  is the concentration of  $\text{H}_2\text{O}_2$  substrate.

## 2.9 Antibacterial experiments

*E. coli*, a representative Gram-negative bacterium, and *S. aureus*, a representative Gram-positive bacterium, were used in the antibacterial experiments. The bacterial suspension (500  $\mu\text{L}$ ,  $1.0 \times 10^7$  CFU per mL) was mixed with the prepared sample solution (500  $\mu\text{L}$ , 200  $\mu\text{g mL}^{-1}$ ) in 48-well plates, respectively. Control groups included  $-\text{H}_2\text{O}_2$  and  $-\text{NIR}$ , while the experimental groups comprised  $+\text{H}_2\text{O}_2$ ,  $+\text{NIR}$ , and  $+\text{H}_2\text{O}_2 + \text{NIR}$ . Each group consisted of three parallel samples. Afterwards, each sample was diluted and uniformly spread onto Luria-Bertani (LB) agar plates, which were then incubated at 37 °C overnight. The bacterial survival rate was calculated using the following formula:

$$\text{Survival rate (\%)} = \text{AE/AC} \times 100\%$$

where AC represents the bacterial concentration (CFU per mL) in the control group and AE represents the bacterial concentration (CFU per mL) in the experimental group.<sup>34</sup>

Under the same conditions, each group of bacteria was centrifuged at 8000 rpm for 3 min, and washed twice with 0.85% NaCl solution. The bacterial suspension was then prepared by dispersing the pellet in 0.85% NaCl solution. The bacteria were stained with working solutions A and B of the Live and Dead Bacteria Staining Kit. After incubation for 20 min, the bacteria were examined under a fluorescence microscope.

Under the same conditions as described above, bacterial samples from each group underwent centrifugation and were fixed in a 2.5% glutaraldehyde solution for 12 h. Subsequently, dehydration was performed sequentially using ethanol solutions with concentrations of 30%, 50%, 70%, 80%, 90%, and 95%, with each step lasting 20 min. The samples were then dehydrated twice with 100% ethanol. Finally, the ethanol was replaced with an appropriate amount of *tert*-butanol, and the bacteria were observed using SEM.

# 3 Results and discussion

## 3.1 Structure characterization

As shown in Fig. 1a,  $\text{Ti}_3\text{C}_2$  nanosheets were synthesized *via* HF etching. The TEM image of the  $\text{Ti}_3\text{C}_2/\text{CuWO}_4/\text{Pt}$  composite is presented in Fig. 1b, where Pt nanoparticles are distinctly observed on the surface of  $\text{Ti}_3\text{C}_2$ . The HRTEM image (Fig. 1c)

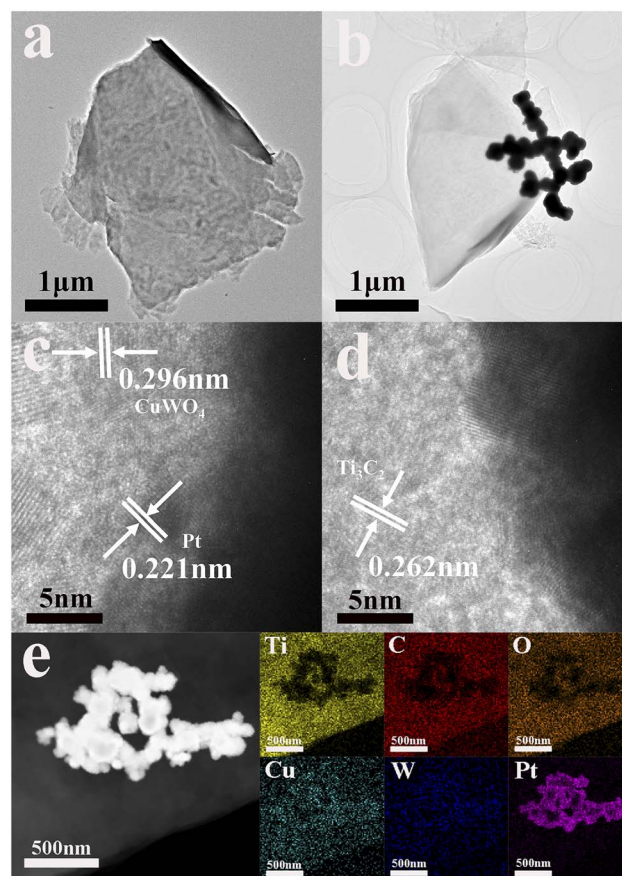


Fig. 1 The TEM images of  $\text{Ti}_3\text{C}_2$  (a) and  $\text{Ti}_3\text{C}_2/\text{CuWO}_4/\text{Pt}$  (b). HRTEM images of  $\text{Ti}_3\text{C}_2/\text{CuWO}_4/\text{Pt}$  (c) and (d). (e) Elemental mappings for  $\text{Ti}_3\text{C}_2/\text{CuWO}_4/\text{Pt}$ .



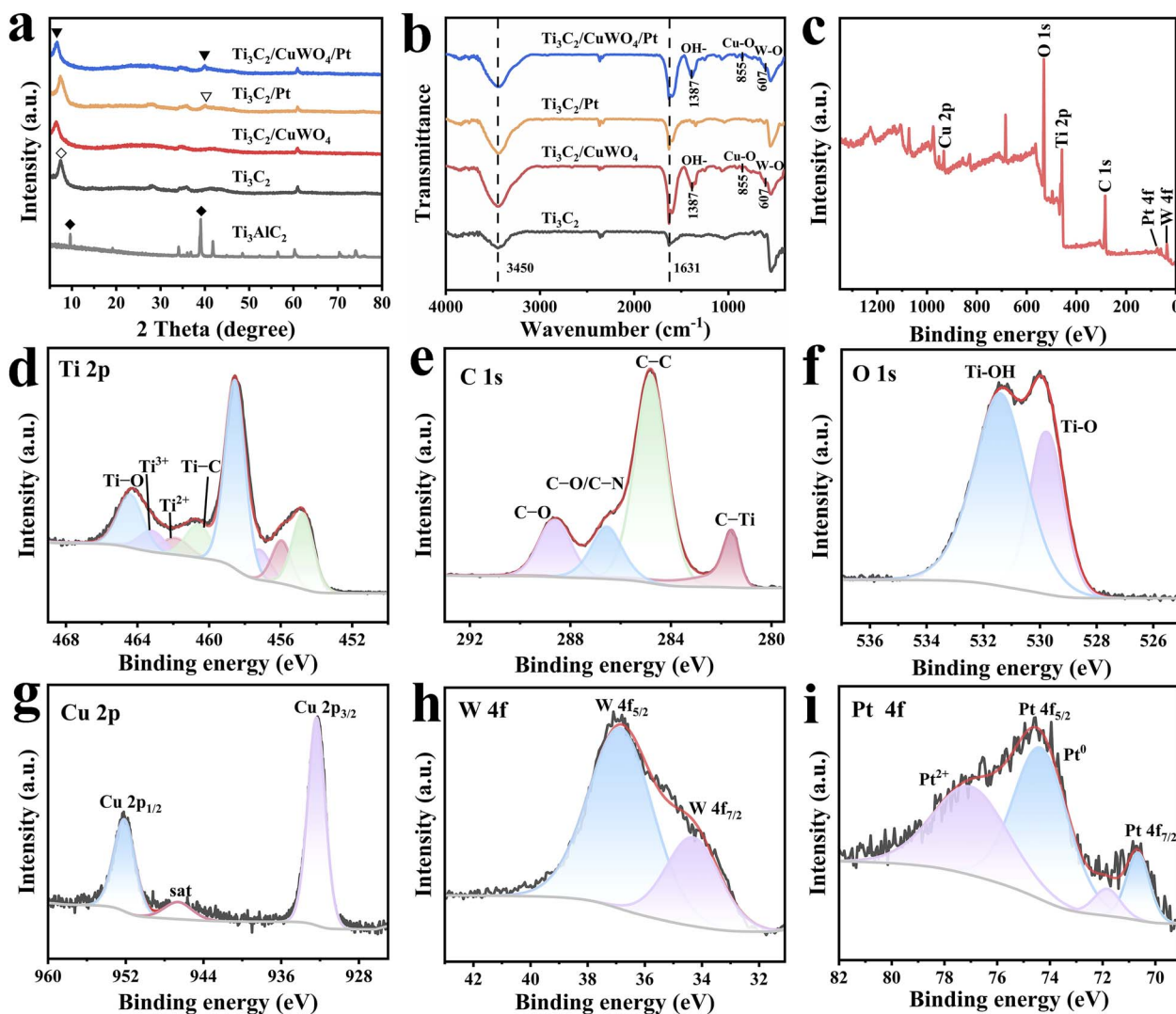


Fig. 2 (a) XRD patterns of  $\text{Ti}_3\text{C}_2$ ,  $\text{Ti}_3\text{C}_2/\text{CuWO}_4$ ,  $\text{Ti}_3\text{C}_2/\text{Pt}$ ,  $\text{Ti}_3\text{C}_2/\text{CuWO}_4/\text{Pt}$ . (b) FTIR spectra of  $\text{Ti}_3\text{C}_2$ ,  $\text{Ti}_3\text{C}_2/\text{CuWO}_4$ ,  $\text{Ti}_3\text{C}_2/\text{Pt}$ ,  $\text{Ti}_3\text{C}_2/\text{CuWO}_4/\text{Pt}$ . (c) XPS spectra of  $\text{Ti}_3\text{C}_2/\text{CuWO}_4/\text{Pt}$ . (d) Ti 2p, (e) C 1s, (f) O 1s, (g) Cu 2p, (h) W 4f, and (i) Pt 4f XPS spectra of  $\text{Ti}_3\text{C}_2/\text{CuWO}_4/\text{Pt}$ .

reveals a lattice spacing of 0.296 nm for  $\text{CuWO}_4$ , corresponding to the distances of the (111) facets of the triclinic  $\text{CuWO}_4$  structure.<sup>35,36</sup> The spacing between adjacent lattice planes is 0.221 nm, which corresponds to the (111) crystal plane of Pt.<sup>37</sup> The lattice stripe of  $\text{Ti}_3\text{C}_2$  is 0.262 nm corresponding to the (0110) crystal plane (Fig. 1d).<sup>38</sup> Furthermore, element mapping confirms the existence of Ti, C, O, Cu, W, and Pt (Fig. 1e), while Cu, W, and Pt are shown to be homogeneously distributed on the surface of  $\text{Ti}_3\text{C}_2$ . The XRD patterns provide crystallographic information for various materials (Fig. 2a). In the XRD pattern of  $\text{Ti}_3\text{AlC}_2$ , a strong (104) peak appears at approximately  $39^\circ$ , while in the  $\text{Ti}_3\text{C}_2$  pattern, the disappearance of this main peak indicates the removal of the aluminium layer. Additionally, the appearance of a peak just before the (002) peak at approximately  $9^\circ$  suggests that the incorporation of lithium ions has increased the interlayer spacing between adjacent  $\text{Ti}_3\text{C}_2$  layers. Thus, the disappearance of the (104) peak, along with the shift in the (002) peak, confirms the successful synthesis of  $\text{Ti}_3\text{C}_2$ .<sup>39</sup>

The XRD patterns of pure  $\text{CuWO}_4$  exhibit broad peaks, characteristic of amorphous structures or very small nanoparticles with limited crystallinity (Fig. S1†). This characteristic promotes the release of  $\text{Cu}^{2+}$  ion. As a result,  $\text{Ti}_3\text{C}_2/\text{CuWO}_4/\text{Pt}$  exhibits broad peaks within the  $20\text{--}30^\circ$  range (Fig. 2a). Additionally, the  $\text{Ti}_3\text{C}_2/\text{CuWO}_4/\text{Pt}$  loaded with platinum nanoparticles exhibits the characteristic peak of platinum, corresponding to the peak around  $40^\circ$  in PDF no. 04-0802, confirming the successful loading of platinum.<sup>40</sup>

The FTIR of  $\text{Ti}_3\text{C}_2/\text{CuWO}_4/\text{Pt}$  shown in Fig. 2b displays a stretching vibration of  $-\text{OH}$  at  $3450\text{ cm}^{-1}$ .<sup>41–43</sup> Additionally, a peak at  $1631\text{ cm}^{-1}$  corresponds to the  $\text{C}-\text{O}$  stretching vibration was observed.<sup>44</sup> Meanwhile,  $\text{Cu}-\text{O}$  and  $\text{W}-\text{O}$  bands were observed at  $855$  and  $607\text{ cm}^{-1}$ , respectively.<sup>45</sup>

Then, XPS was conducted to characterize the material's elemental composition and chemical states. As depicted in Fig. 2c, the results confirm the existence of Ti, C, O, Cu, W, and Pt elements within  $\text{Ti}_3\text{C}_2/\text{CuWO}_4/\text{Pt}$ . The high-resolution XPS spectrum of Ti 2p revealed four distinct pairs of Ti  $2p_{3/2}$



and Ti 2p<sub>1/2</sub> peaks located at 454.8/460.6, 456.0/461.9, 457.2/463.2, and 458.6/464.4 eV, corresponding to the chemical states of Ti-C, Ti<sup>2+</sup>, Ti<sup>3+</sup>, and Ti-O, respectively (Fig. 2d).<sup>46,47</sup> In the C 1s spectra (Fig. 2e), the peaks at 281.6, 284.8, 286.6, and 288.6 eV were assigned to C-Ti, C-C, C-O/C-N, and C=O species, respectively.<sup>48</sup> In the O 1s region, the peaks at 529.7 and 531.4 eV are attributed to Ti-O and Ti-OH species (Fig. 2f).<sup>49</sup> The Cu 2p spectrum displayed peaks at approximately 932.4 and 952.14 eV, corresponding to Cu(II) 2p<sub>3/2</sub> and Cu(II) 2p<sub>1/2</sub> in CuWO<sub>4</sub> (Fig. 2g).<sup>50</sup> For the tungsten element (Fig. 2h), the binding energies near 34.3 and 36.8 eV were assigned to W 4f<sub>7/2</sub> and W 4f<sub>5/2</sub> of W(VI) in CuWO<sub>4</sub>.<sup>51,52</sup> The high-resolution Pt 4f spectrum (Fig. 2i) exhibits two distinct peaks at binding energies of approximately 74.3 and 70.7 eV, which are attributed to 4f<sub>5/2</sub> and 4f<sub>7/2</sub>, respectively. The two peaks can further be separated into two sets of peaks, which correspond to Pt<sup>2+</sup> and Pt<sup>0</sup>.<sup>53</sup> Overall, the XPS analysis provides detailed information on the valence bond structure of each constituent in Ti<sub>3</sub>C<sub>2</sub>/CuWO<sub>4</sub>/Pt and confirms the stable presence of all components in the final product.

### 3.2 Photothermal property

The photothermal properties of Ti<sub>3</sub>C<sub>2</sub>/CuWO<sub>4</sub>/Pt were initially assessed by measuring the absorbance of the different materials (Fig. 3a). The results indicated that all tested materials exhibited strong absorption at 808 nm. Therefore, the photothermal heating rates of different samples were investigated under 808 nm laser exposure. According to the heating temperature profiles of various materials (Fig. 3b), the temperatures of Ti<sub>3</sub>C<sub>2</sub>, Ti<sub>3</sub>C<sub>2</sub>/CuWO<sub>4</sub>, Ti<sub>3</sub>C<sub>2</sub>/Pt and Ti<sub>3</sub>C<sub>2</sub>/CuWO<sub>4</sub>/Pt with a concentration of 100 µg mL<sup>-1</sup> were significantly increased under 10 min of continuous NIR laser exposure (1.09 W cm<sup>-2</sup>), rising from 27.8 °C to 74.2, 73.3, 70.7, and 72.7 °C, respectively. The photothermal images were shown in Fig. S2†. Notably, the addition of CuWO<sub>4</sub> and Pt appeared to slightly reduce the temperature increase, potentially due to the influence of Ti<sub>3</sub>C<sub>2</sub> surface capping material on the photothermal effect.

The impact of power intensity on the photothermal efficiency was further investigated by exposing Ti<sub>3</sub>C<sub>2</sub>/CuWO<sub>4</sub>/Pt solutions (100 µg mL<sup>-1</sup>) to gradient power densities (0.49, 1.09,

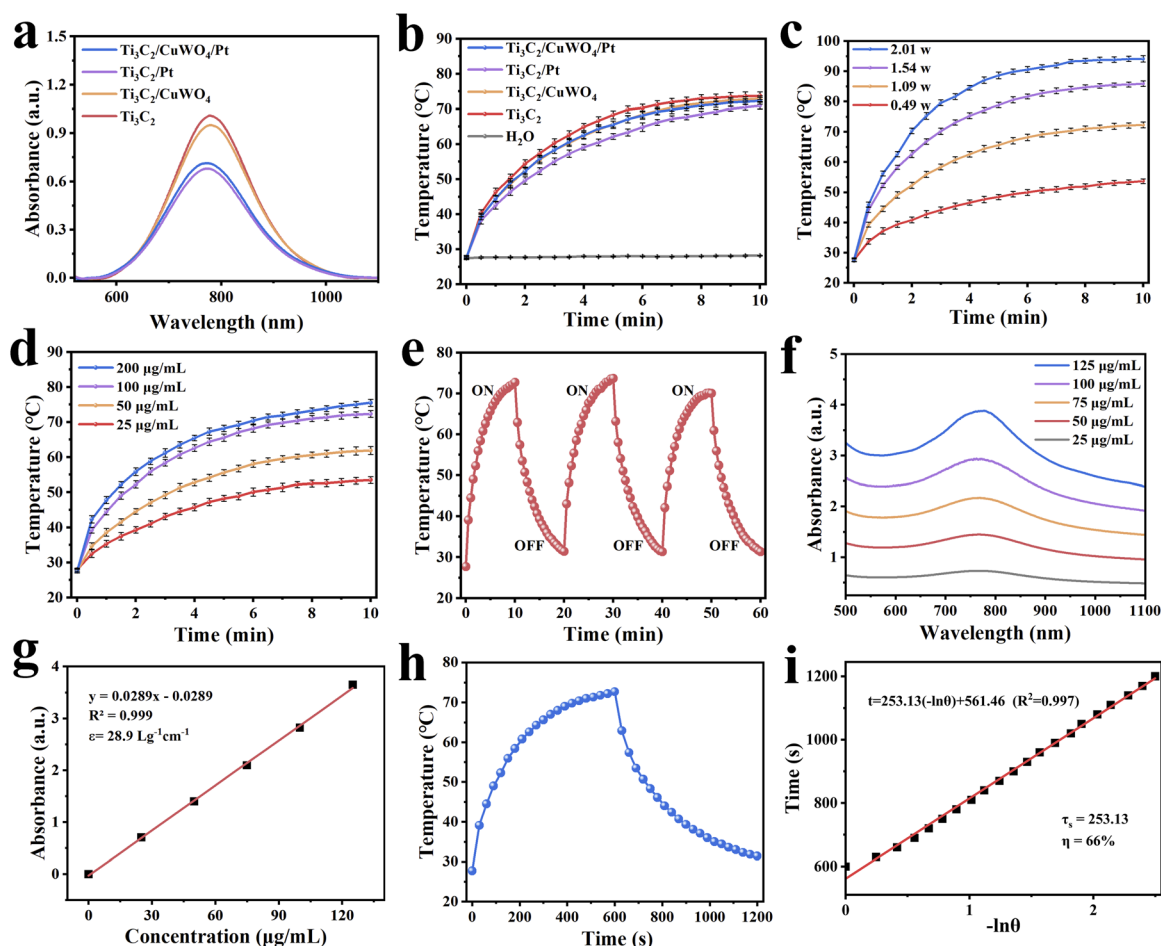


Fig. 3 (a) UV-vis absorption spectra of Ti<sub>3</sub>C<sub>2</sub>, Ti<sub>3</sub>C<sub>2</sub>/CuWO<sub>4</sub>, Ti<sub>3</sub>C<sub>2</sub>/Pt, and Ti<sub>3</sub>C<sub>2</sub>/CuWO<sub>4</sub>/Pt. (b) Photothermal heating curves of Ti<sub>3</sub>C<sub>2</sub>, Ti<sub>3</sub>C<sub>2</sub>/CuWO<sub>4</sub>, Ti<sub>3</sub>C<sub>2</sub>/Pt, and Ti<sub>3</sub>C<sub>2</sub>/CuWO<sub>4</sub>/Pt with 808 nm laser. Photothermal heating curves of Ti<sub>3</sub>C<sub>2</sub>/CuWO<sub>4</sub>/Pt by 808 nm laser at different (c) power densities and (d) concentrations. (e) Photothermal stability of Ti<sub>3</sub>C<sub>2</sub>/CuWO<sub>4</sub>/Pt (three cycles of laser on/off) under 808 nm laser illumination. (f) UV-vis absorption spectra of Ti<sub>3</sub>C<sub>2</sub>/CuWO<sub>4</sub>/Pt at different concentrations. (g) The mass extinction coefficient of Ti<sub>3</sub>C<sub>2</sub>/CuWO<sub>4</sub>/Pt at 808 nm, and normalized absorbance intensity at varied concentrations. (h) Heating and cooling curves of Ti<sub>3</sub>C<sub>2</sub>/CuWO<sub>4</sub>/Pt. (i) Linear time data versus  $-\ln(\theta)$  obtained from the cooling period.





1.54, and  $2.01 \text{ W cm}^{-2}$ ). Fig. 3c shows that the group exposed to  $0.49 \text{ W cm}^{-2}$  exhibited the lowest temperature increase, from  $27.5^\circ\text{C}$  to  $53.4^\circ\text{C}$ . When the power intensity was raised to  $1.09 \text{ W cm}^{-2}$ , the peak temperature reached  $72.7^\circ\text{C}$ . Similarly, the  $2.01 \text{ W cm}^{-2}$  group achieved a maximum temperature of  $93.8^\circ\text{C}$ . Based on these results,  $1.09 \text{ W cm}^{-2}$  was determined to be the optimal power intensity.

Following the investigation into the relationship between power intensity and photothermal properties, material solutions with varying concentrations ( $25, 50, 100$ , and  $200 \mu\text{g mL}^{-1}$ ) were exposed individually to an NIR laser ( $1.09 \text{ W cm}^{-2}$ ) to examine the correlation between sample concentration and photothermal performance. As depicted in Fig. 3d, the final temperatures of the  $25, 50, 100$ , and  $200 \mu\text{g mL}^{-1}$  groups increased from  $27.7^\circ\text{C}$  to  $53.3, 61.7, 72.7$ , and  $75.5^\circ\text{C}$ , respectively. These results indicate that higher material concentrations lead to improved photothermal efficiency.

Collectively, the results suggest that the final temperature can be adjusted by tuning the material concentration and the NIR laser's power intensity. Additionally, the photothermal stability of  $\text{Ti}_3\text{C}_2/\text{CuWO}_4/\text{Pt}$  was confirmed through cycling tests. During repeated cycles, the maximum temperature still

stabilized around  $70^\circ\text{C}$  (Fig. 3e), indicating the excellent photothermal stability of  $\text{Ti}_3\text{C}_2/\text{CuWO}_4/\text{Pt}$ .

It can be seen from Fig. 3f that  $\text{Ti}_3\text{C}_2/\text{CuWO}_4/\text{Pt}$  solutions with different concentrations ( $25, 50, 75, 100$ , and  $125 \mu\text{g mL}^{-1}$ ) display measurable absorption at  $808 \text{ nm}$ . The evaluation of photothermal conversion performance primarily relies on two critical parameters: the extinction coefficient ( $\epsilon$ ) and photothermal conversion efficiency ( $\eta$ ). According to the Lambert–Beer law, the extinction coefficient of  $\text{Ti}_3\text{C}_2/\text{CuWO}_4/\text{Pt}$  at  $808 \text{ nm}$  was calculated to be  $28.9 \text{ L (g}^{-1} \text{ cm}^{-1})$  (Fig. 3g). The theoretical photothermal conversion efficiency of  $\text{Ti}_3\text{C}_2/\text{CuWO}_4/\text{Pt}$  was determined to be  $66\%$  (Fig. 3h and i), indicating that it is a highly efficient photothermal conversion material. Therefore, the comprehensive results confirm the potential of  $\text{Ti}_3\text{C}_2/\text{CuWO}_4/\text{Pt}$  as a photothermal agent for antibacterial treatment.

### 3.3 Analysis of released $\text{Cu}^{2+}$ ions

The effect of light exposure on  $\text{Cu}^{2+}$  ion release was further investigated. The  $\text{Cu}^{2+}$  ion concentrations in the dialysis solution were determined using ICP-OES, which revealed that the release of  $\text{Cu}^{2+}$  ions from  $\text{Ti}_3\text{C}_2/\text{CuWO}_4/\text{Pt}$  increased by  $92.6\%$  after light exposure compared to the non-illuminated condition (Table 1).

### 3.4 Peroxidase-like property

In this study, TMB was used as the substrate, and the photothermal enhancement of POD-like activity was investigated under the conditions of  $\text{H}_2\text{O}_2$  presence and NIR laser irradiation (Fig. 4a). Additionally, the catalytic capabilities of  $\text{H}_2\text{O}_2$  were compared between  $\text{Ti}_3\text{C}_2$  combined with single-component

Table 1 Increase rate of  $\text{Cu}^{2+}$  ions after NIR light illumination

Condition	Increase rate
NIR (–)	0.0%
NIR (+)	92.6%

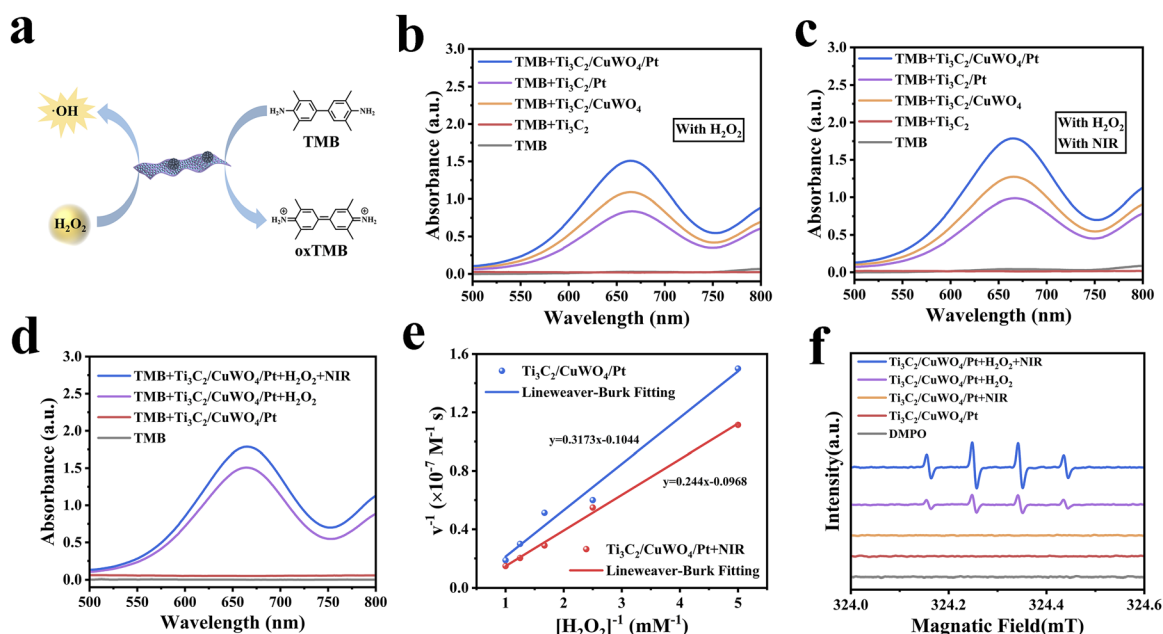


Fig. 4 (a) Schematic illustration of chemical reaction in oxidation of TMB. (b) UV-vis absorption spectra of  $\text{Ti}_3\text{C}_2$ ,  $\text{Ti}_3\text{C}_2/\text{CuWO}_4$ ,  $\text{Ti}_3\text{C}_2/\text{Pt}$ , and  $\text{Ti}_3\text{C}_2/\text{CuWO}_4/\text{Pt}$  the catalysed TMB under addition of  $\text{H}_2\text{O}_2$ . (c) UV-vis absorption spectra of  $\text{Ti}_3\text{C}_2$ ,  $\text{Ti}_3\text{C}_2/\text{CuWO}_4$ ,  $\text{Ti}_3\text{C}_2/\text{Pt}$ , and  $\text{Ti}_3\text{C}_2/\text{CuWO}_4/\text{Pt}$  the catalysed TMB under addition of  $\text{H}_2\text{O}_2$  and NIR conditions. (d) UV-vis absorption spectra of  $\text{Ti}_3\text{C}_2/\text{CuWO}_4/\text{Pt}$  catalysed TMB under different conditions. (e) Lineweaver–Burk fitted (double inversions) curves before and after illumination. (f) ESR spectra with DMPO as the spin-trapping agent under different conditions.

nanozymes and a hybrid nanozyme composed of photothermal agents and nanozymes. All materials did not respond without the addition of  $\text{H}_2\text{O}_2$  (Fig. S3†). As shown in Fig. 4b, after adding  $\text{H}_2\text{O}_2$ , neither the control group nor the  $\text{Ti}_3\text{C}_2$  group displayed obvious absorption peaks at 652 nm, indicating that  $\text{Ti}_3\text{C}_2$  did not exhibit POD-like activity. However, the absorbance spectra of the TMB solutions for the  $\text{Ti}_3\text{C}_2/\text{CuWO}_4$ ,  $\text{Ti}_3\text{C}_2/\text{Pt}$ , and  $\text{Ti}_3\text{C}_2/\text{CuWO}_4/\text{Pt}$  groups all exhibited a distinct absorption peak around 652 nm, indicating that all three systems were able to catalyse  $\text{H}_2\text{O}_2$  through a Fenton-like reaction to generate  $\cdot\text{OH}$  with characteristic chemodynamic properties. Notably, the  $\text{Ti}_3\text{C}_2/\text{CuWO}_4/\text{Pt}$  nanozyme exhibited higher catalytic activity compared to the  $\text{Ti}_3\text{C}_2/\text{CuWO}_4$  and  $\text{Ti}_3\text{C}_2/\text{Pt}$  single-component nanozymes. In Fig. 4c, NIR irradiation significantly enhanced the catalytic performance of all nanozymes, with the  $\text{Ti}_3\text{C}_2/\text{CuWO}_4/\text{Pt}$  nanozyme still exhibiting the strongest catalytic ability. Fig. 4d demonstrates that the catalytic performance of  $\text{Ti}_3\text{C}_2/\text{CuWO}_4/\text{Pt}$  was further improved by the addition of NIR light irradiation.

To explore more intuitively the photothermal enhancement of enzyme activity using  $\text{Ti}_3\text{C}_2/\text{CuWO}_4/\text{Pt}$ , we investigated the

affinity of  $\text{Ti}_3\text{C}_2/\text{CuWO}_4/\text{Pt}$  for the substrate of the  $\text{H}_2\text{O}_2$  reaction before and after illumination, as well as the catalytic reaction rate at varying  $\text{H}_2\text{O}_2$  concentrations. Using the Lineweaver–Burk model, while maintaining the TMB concentration and adjusting the  $\text{H}_2\text{O}_2$  concentration, key kinetic parameters were derived.

The  $K_m$  value for  $\text{Ti}_3\text{C}_2/\text{CuWO}_4/\text{Pt}$  was determined as 2.941 mM, and the  $V_{\text{max}}$  value was  $12.9 \times 10^{-7} \text{ M s}^{-1}$  after illumination (Fig. 4e). Compared with that before illumination,  $\text{Ti}_3\text{C}_2/\text{CuWO}_4/\text{Pt}$  demonstrates an enhanced affinity for the enzyme and an improved catalytic rate towards the substrate  $\text{H}_2\text{O}_2$ . Based on the above analysis,  $\text{Ti}_3\text{C}_2/\text{CuWO}_4/\text{Pt}$  has excellent photothermal enhanced POD-like catalytic activity. Meanwhile, the production and photothermal enhancement of  $\cdot\text{OH}$  was also confirmed by the ESR analysis using 5,5dimethyl-1-pyrroline-*N*-oxide (DMPO) as the  $\cdot\text{OH}$  trapping agent. DMPO reacts with  $\cdot\text{OH}$  to generate DMPO/OH adducts, resulting in four characteristics peaks in the ESR spectrum, confirming the existence of  $\cdot\text{OH}$ . As can be seen in Fig. 4f, no distinct signal was detected when the DMPO trapping agent was combined with  $\text{Ti}_3\text{C}_2/\text{CuWO}_4/\text{Pt}$  under light exposure. The photothermal

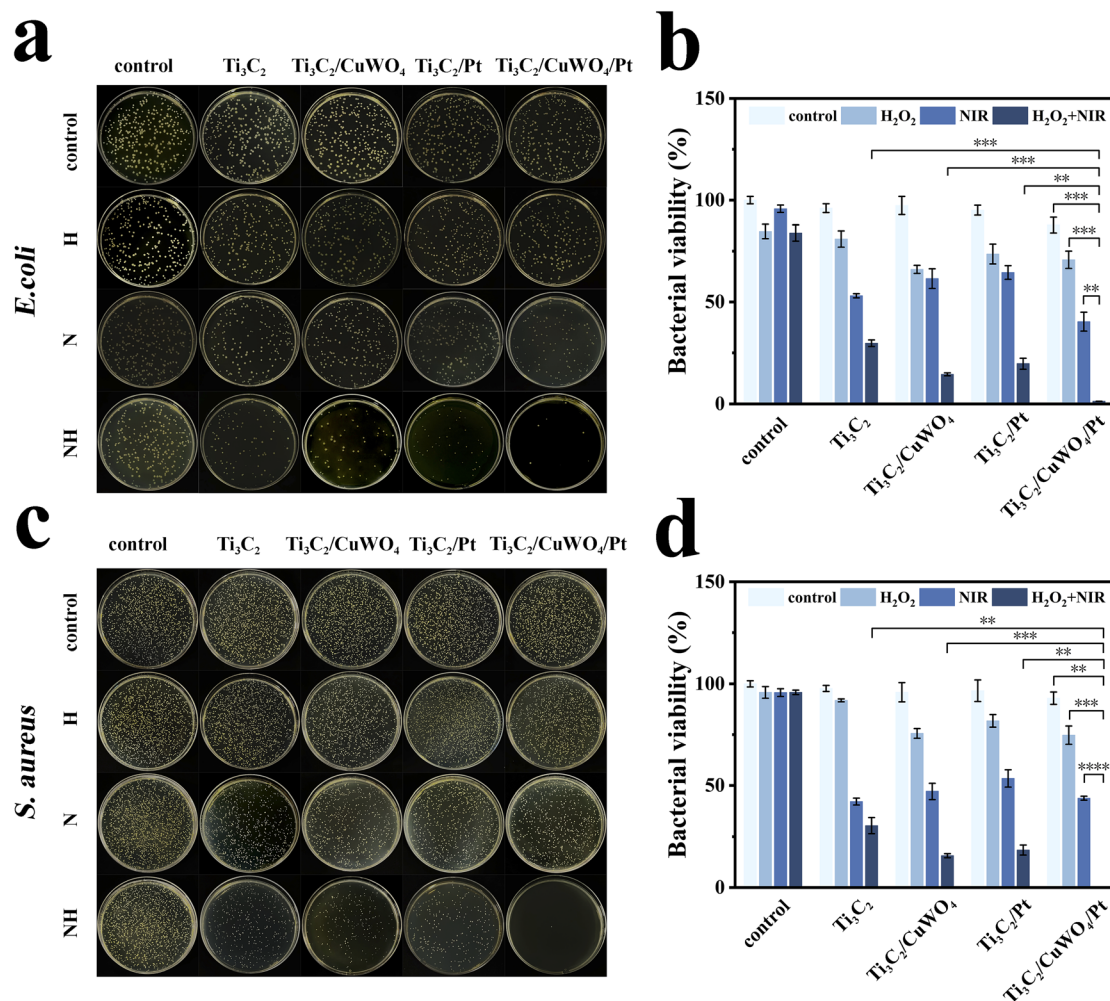


Fig. 5 Photographs of (a) *E. coli* and (c) *S. aureus* colonies formed by  $\text{Ti}_3\text{C}_2$ ,  $\text{Ti}_3\text{C}_2/\text{CuWO}_4$ ,  $\text{Ti}_3\text{C}_2/\text{Pt}$ , and  $\text{Ti}_3\text{C}_2/\text{CuWO}_4/\text{Pt}$  under  $+\text{H}_2\text{O}_2$ ,  $+\text{NIR}$ , and  $+\text{H}_2\text{O}_2 + \text{NIR}$  conditions; relative survival of (b) *E. coli* and (d) *S. aureus*. Data were given as mean  $\pm$  SD ( $n = 3$ ,  $**p < 0.01$ ,  $***p < 0.001$ ,  $****p < 0.0001$ ).



condition failed to produce  $\cdot\text{OH}$ , whereas the introduction of  $\text{H}_2\text{O}_2$  led to the appearance of four distinct peaks with an intensity ratio of approximately 1 : 2 : 2 : 1 in the ESR spectra. This result indicates that  $\text{Ti}_3\text{C}_2/\text{CuWO}_4/\text{Pt}$  could effectively facilitate the breakdown of  $\text{H}_2\text{O}_2$  to produce  $\cdot\text{OH}$ . Following the addition of  $\text{H}_2\text{O}_2$  under light exposure, the four characteristic signal lines were significantly enhanced, clearly demonstrating the photothermal enhancement of  $\cdot\text{OH}$  generation. The ESR results further revealed that  $\text{Ti}_3\text{C}_2/\text{CuWO}_4/\text{Pt}$  can produce  $\cdot\text{OH}$ , which plays a crucial role in the nanozyme catalytic process.

### 3.5 Evaluation of antimicrobial properties

To further investigate the antimicrobial activity of  $\text{Ti}_3\text{C}_2/\text{CuWO}_4/\text{Pt}$  photothermally enhanced nanozyme catalytic activity, we utilized *E. coli*, and *S. aureus* as microbial models, employing the plate counting method. The research elucidates the impact of  $+\text{H}_2\text{O}_2$ ,  $+\text{NIR}$  irradiation, and combined  $+\text{H}_2\text{O}_2 +$

NIR irradiation on the antibacterial properties of four materials:  $\text{Ti}_3\text{C}_2$ ,  $\text{Ti}_3\text{C}_2/\text{CuWO}_4$ ,  $\text{Ti}_3\text{C}_2/\text{Pt}$ , and  $\text{Ti}_3\text{C}_2/\text{CuWO}_4/\text{Pt}$ . According to Fig. S4,<sup>†</sup> the minimum inhibitory concentration (MIC) of  $\text{Ti}_3\text{C}_2/\text{CuWO}_4/\text{Pt}$  against *E. coli* is about  $25\ \mu\text{g mL}^{-1}$ , with an NIR irradiation time of 5 min.  $\text{CuWO}_4$  and Pt were individually used as control groups, as shown in Fig. S6a.<sup>†</sup> The  $+\text{NIR}$  treatment alone had minimal impact, whereas the bacterial survival rates in the  $+\text{H}_2\text{O}_2 + \text{NIR}$  group were  $73.5 \pm 4.0\%$  and  $79.6 \pm 3.9\%$ , respectively (Fig. S6b<sup>†</sup>). In Fig. 5a, a slight reduction in the colony count was observed in the  $+\text{H}_2\text{O}_2$  group, and an obvious decrease in colony count was noted in the  $+\text{NIR}$  group relative to the control, with survival rates of  $53.1 \pm 1.0\%$  for the  $\text{Ti}_3\text{C}_2$  group,  $61.5 \pm 4.8\%$  for the  $\text{Ti}_3\text{C}_2/\text{CuWO}_4$  group,  $64.5 \pm 3.4\%$  for the  $\text{Ti}_3\text{C}_2/\text{Pt}$  group, and  $40.3 \pm 4.7\%$  for the  $\text{Ti}_3\text{C}_2/\text{CuWO}_4/\text{Pt}$  group. This suggests that photothermal antimicrobial capacity is more effective than chemodynamics. The most prominent effect was observed in the  $+\text{H}_2\text{O}_2 + \text{NIR}$  group, where the  $\text{Ti}_3\text{C}_2/$

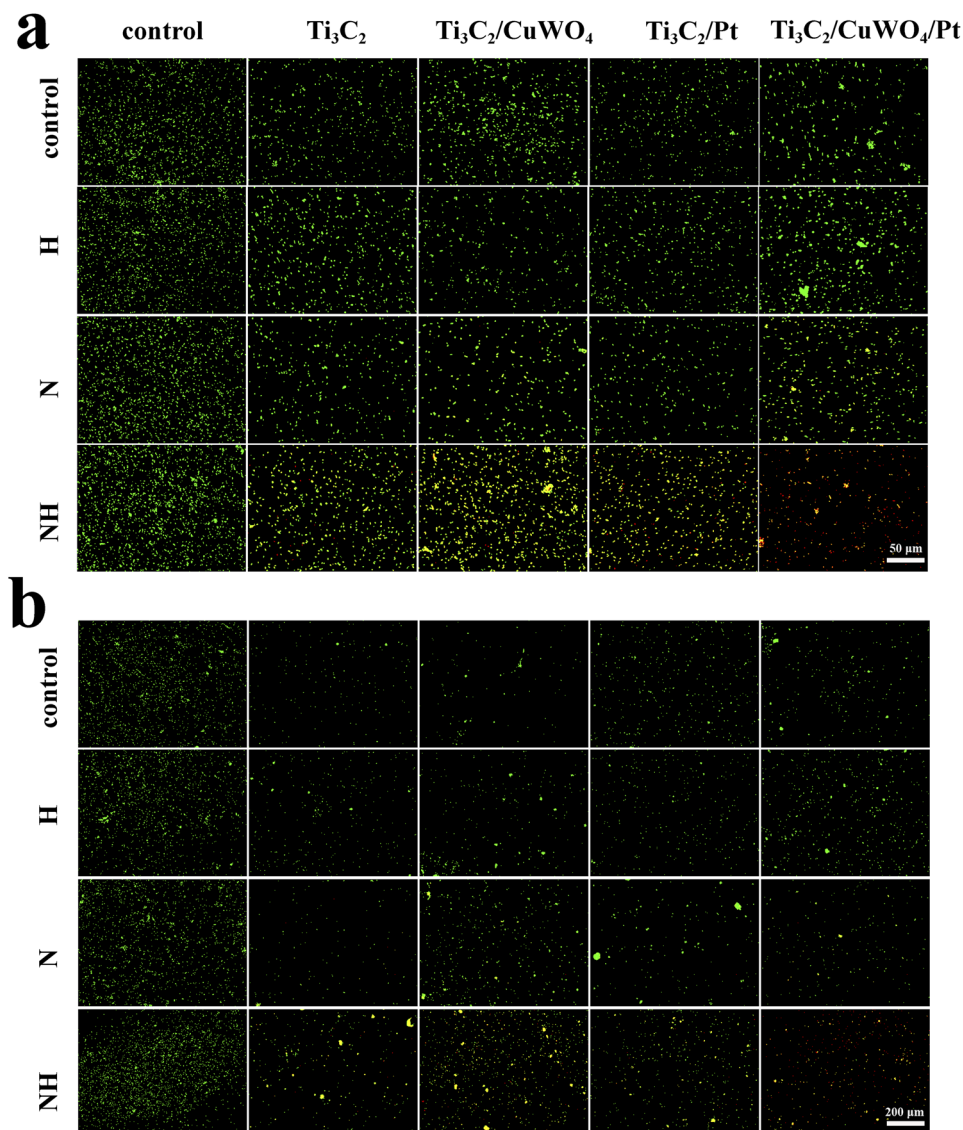


Fig. 6 Fluorescence staining images of (a) *E. coli* and (b) *S. aureus* for  $\text{Ti}_3\text{C}_2$ ,  $\text{Ti}_3\text{C}_2/\text{CuWO}_4$ ,  $\text{Ti}_3\text{C}_2/\text{Pt}$ , and  $\text{Ti}_3\text{C}_2/\text{CuWO}_4/\text{Pt}$  under  $+\text{H}_2\text{O}_2$ ,  $+\text{NIR}$ , and  $+\text{H}_2\text{O}_2 + \text{NIR}$  conditions.

CuWO<sub>4</sub>/Pt exhibited an almost complete absence of colonies. This indicates that photothermal enhances the antibacterial efficiency of nanozyme catalytic activity. Under the combined +H<sub>2</sub>O<sub>2</sub> +NIR conditions, Ti<sub>3</sub>C<sub>2</sub>/CuWO<sub>4</sub> (survival rate of 14.6 ± 0.7%) and Ti<sub>3</sub>C<sub>2</sub>/Pt (survival rate of 19.7 ± 2.6%) demonstrated superior antibacterial activity compared to Ti<sub>3</sub>C<sub>2</sub> (survival rate of 29.7 ± 1.6%), indicating that single-component nanozyme could enhance antibacterial ability to a certain extent, but the effect was not optimal. The survival rate of Ti<sub>3</sub>C<sub>2</sub>/CuWO<sub>4</sub>/Pt against *E. coli* was only 1.3 ± 0.2% (Fig. 5b).

For *S. aureus*, the MIC of Ti<sub>3</sub>C<sub>2</sub>/CuWO<sub>4</sub>/Pt was about 50 µg mL<sup>-1</sup> at an NIR irradiation time of 4 min (Fig. S5†). Under this condition, the antibacterial trend was similar to that of *E. coli*. Meanwhile, CuWO<sub>4</sub> and Pt were separately used as control groups in Fig. S6c.† The addition of NIR alone showed little effect, while the bacterial survival rates in the +H<sub>2</sub>O<sub>2</sub> +NIR group were 63.8 ± 2.7% and 77.7 ± 1.5%, respectively (Fig. S6d.†). As illustrated in the control group in Fig. 5c, there was little change in the number of colonies treated with H<sub>2</sub>O<sub>2</sub> and NIR. In the

+H<sub>2</sub>O<sub>2</sub> group, the colony survival rate of Ti<sub>3</sub>C<sub>2</sub>/CuWO<sub>4</sub>, Ti<sub>3</sub>C<sub>2</sub>/Pt, and Ti<sub>3</sub>C<sub>2</sub>/CuWO<sub>4</sub>/Pt decreased to approximately 80%. This reduction was ascribed to the nanozyme catalytic function, which boosted the production of ·OH from H<sub>2</sub>O<sub>2</sub>, thereby exerting a bactericidal effect (Fig. 5d). In the +NIR group, all four materials have good antibacterial effects, with survival rates of 42.3 ± 1.69% for the Ti<sub>3</sub>C<sub>2</sub> group, 47.2 ± 3.9% for the Ti<sub>3</sub>C<sub>2</sub>/CuWO<sub>4</sub> group, 53.5 ± 4.3% for the Ti<sub>3</sub>C<sub>2</sub>/Pt group, and 43.9 ± 1.0% for the Ti<sub>3</sub>C<sub>2</sub>/CuWO<sub>4</sub>/Pt group. In the +H<sub>2</sub>O<sub>2</sub> +NIR group, the bacterial survival rate decreased to 15.6 ± 1.0% and 18.4 ± 2.5% in the Ti<sub>3</sub>C<sub>2</sub>/CuWO<sub>4</sub> and Ti<sub>3</sub>C<sub>2</sub>/Pt groups, respectively. And bacterial survival in the Ti<sub>3</sub>C<sub>2</sub>/CuWO<sub>4</sub>/Pt group was nearly zero. This finding not only indicates the effectiveness of the photothermal-enhanced nanozyme catalytic antibacterial activity, but also highlights the superior antibacterial activity of hybrid nanozymes composed of photothermal agents compared to single-component nanozymes.

To visually examine antibacterial effects under various treatments, bacteria were stained with DMAO/EthD-III and

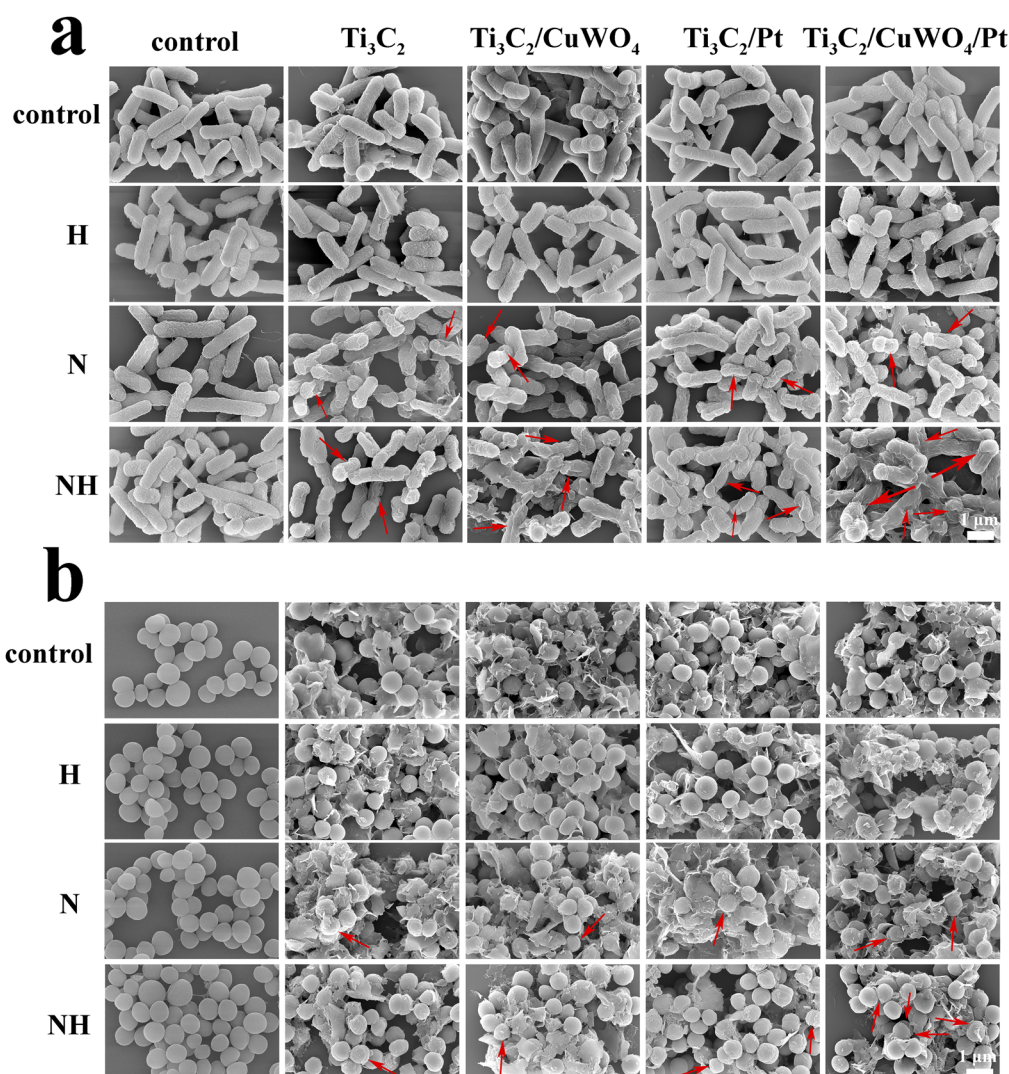


Fig. 7 SEM images of (a) *E. coli* and (b) *S. aureus* for Ti<sub>3</sub>C<sub>2</sub>, Ti<sub>3</sub>C<sub>2</sub>/CuWO<sub>4</sub>, Ti<sub>3</sub>C<sub>2</sub>/Pt, and Ti<sub>3</sub>C<sub>2</sub>/CuWO<sub>4</sub>/Pt under +H<sub>2</sub>O<sub>2</sub>, +NIR, and +H<sub>2</sub>O<sub>2</sub> +NIR conditions.



visualized using fluorescence microscopy. Live bacteria showed green fluorescence, while dead bacteria emitted red fluorescence Fig. 6a and b shows that all the *E. coli* and *S. aureus* were marked green in the control group, regardless of H<sub>2</sub>O<sub>2</sub> addition or NIR laser exposure. Only a few dead bacteria labelled in red were observed in the +H<sub>2</sub>O<sub>2</sub> alone and +NIR alone groups. On the contrary, most of the Ti<sub>3</sub>C<sub>2</sub>, Ti<sub>3</sub>C<sub>2</sub>/CuWO<sub>4</sub>, and Ti<sub>3</sub>C<sub>2</sub>/Pt groups showed yellow fluorescence, representing a mixture of live and dead bacteria under +H<sub>2</sub>O<sub>2</sub> +NIR conditions. Notably, almost all bacteria in the Ti<sub>3</sub>C<sub>2</sub>/CuWO<sub>4</sub>/Pt group showed red fluorescence, suggesting widespread bacterial death. This is aligned with results from diffusion plate counting, proving their great potential against *E. coli* and *S. aureus*.

Furthermore, the morphology of the two bacterial strains under different treatments was characterized using SEM. As shown in Fig. 7a and b, *E. coli* showed a capsule-like structure and *S. aureus* showed irregular spheres with smooth surfaces. Bacteria in the control group maintained their structural integrity, while +H<sub>2</sub>O<sub>2</sub> treatment caused negligible changes to those in the Ti<sub>3</sub>C<sub>2</sub>/CuWO<sub>4</sub> and Ti<sub>3</sub>C<sub>2</sub>/Pt groups. However, slight wrinkling of bacterial cell membranes was observed in Ti<sub>3</sub>C<sub>2</sub>, Ti<sub>3</sub>C<sub>2</sub>/CuWO<sub>4</sub>, Ti<sub>3</sub>C<sub>2</sub>/Pt, and Ti<sub>3</sub>C<sub>2</sub>/CuWO<sub>4</sub>/Pt groups after +NIR illumination. After combined treatment of +H<sub>2</sub>O<sub>2</sub> +NIR, the Ti<sub>3</sub>C<sub>2</sub>/CuWO<sub>4</sub>, and Ti<sub>3</sub>C<sub>2</sub>/Pt groups exhibited significant deformation and wrinkling. *E. coli* membrane rupture and crumpled *S. aureus* deformation were observed in the Ti<sub>3</sub>C<sub>2</sub>/CuWO<sub>4</sub>/Pt group, which was attributed to the denaturation of proteins and lipids on the membranes by localized heating and the production of ·OH, and the further disruption of the integrity of the bacterial membranes. This suggests that the hybrid nanozyme composed of photothermal agents and nanozymes exhibited the most significant bactericidal efficiency.

These findings indicate that the Ti<sub>3</sub>C<sub>2</sub>/CuWO<sub>4</sub>/Pt nanozyme composite possesses notable advantages in photothermally enhanced nanozyme-catalysed antibacterial activity, underscoring its potential for *in vivo* applications. In contrast to conventional antibiotics, its antibiotic-free antibacterial mechanism can effectively minimise the risk of antibiotic resistance, which opens up new possibilities for the development of antibiotic-free antibacterial strategies.

## 4 Conclusions

In this study, the Ti<sub>3</sub>C<sub>2</sub>/CuWO<sub>4</sub>/Pt nanozyme with excellent photothermal conversion performance and POD-like catalytic activity was synthesized as an effective antimicrobial agent. Facilitated by NIR laser exposure, the material achieved a photothermal conversion efficiency of up to 66%, with its photothermal properties significantly enhancing the peroxidase-like catalytic activity. Additionally, the photothermal effect facilitated the release of Cu<sup>2+</sup> ions from the CuWO<sub>4</sub>, further boosting the catalytic performance of the composite. The Ti<sub>3</sub>C<sub>2</sub>/CuWO<sub>4</sub>/Pt nanoplateform exhibited rapid and efficient antimicrobial activity, effectively inhibiting *E. coli* and *S. aureus* within only 4 to 5 min of NIR light irradiation. Thus, the Ti<sub>3</sub>C<sub>2</sub>/CuWO<sub>4</sub>/Pt composite material leverages photothermal effects to enhance chemodynamic processes, achieving efficient and rapid

bactericidal effects, and demonstrates significant potential for applications in antibiotic-free antimicrobial strategies.

## Data availability

The authors confirm that the data supporting the findings of this study are available within the article [and/or] as its ESI.†

## Conflicts of interest

The authors declare that they have no known competing financial interests or personal relationships that could have appeared to influence the work reported in this paper.

## Acknowledgements

This work was financially supported by the National Natural Science Foundation of China (No. 52262014, 22365013) and the Cooperation Project of Shenjiu Group Co., Ltd. and Sichuan University of Science & Engineering (No. HX2022313).

## References

- 1 B. Tornimbene, S. Eremin, M. Escher, J. Griskeviciene, S. Manghani and C. L. Pessoa-Silva, *Lancet Infect. Dis.*, 2018, **18**, 241–242.
- 2 R. A. Fisher, B. Gollan and S. Helaine, *Nat. Rev. Microbiol.*, 2017, **15**, 453–464.
- 3 A. Abbas, A. Barkhouse, D. Hackenberger and G. D. Wright, *Cell Host Microbe*, 2024, **32**, 837–851.
- 4 R. Laxminarayan, *Lancet*, 2022, **399**, 606–607.
- 5 J. Liu, O. Gefen, I. Ronin, M. Bar-Meir and N. Q. Balaban, *Science*, 2020, **367**, 200–204.
- 6 J. M. V. Makabenta, A. Nabawy, C.-H. Li, S. Schmidt-Malan, R. Patel and V. M. Rotello, *Nat. Rev. Microbiol.*, 2021, **19**, 23–36.
- 7 X. Qi, Y. Xiang, E. Cai, X. Ge, X. Chen, W. Zhang, Z. Li and J. Shen, *Coord. Chem. Rev.*, 2023, **496**, 215426.
- 8 Y. Zou, Y. Zhang, Q. Yu and H. Chen, *Biomater. Sci.*, 2021, **9**, 10–22.
- 9 T. R. Dmytriv and V. I. Lushchak, *Chem. Rec.*, 2024, **24**, e202300338.
- 10 K. Maleski, C. E. Shuck, A. T. Fafarman and Y. Gogotsi, *Adv. Opt. Mater.*, 2021, **9**, 2001563.
- 11 F. Wu, H. Zheng, W. Wang, Q. Wu, Q. Zhang, J. Guo, B. Pu, X. Shi, J. Li, X. Chen and W. Hong, *Sci. China Mater.*, 2021, **64**, 748–758.
- 12 C. Xu, J. Li, C. Ou, J. Yang, S. Fu, W. Hu, L. Wang, Z. Wang, L. Hai, L. Deng and D. He, *Chem. Eng. J.*, 2024, **499**, 156170.
- 13 Q. Tian, F. Xue, Y. Wang, Y. Cheng, L. An, S. Yang, X. Chen and G. Huang, *Nano Today*, 2021, **39**, 101162.
- 14 F. Wei, X. Cui, Z. Wang, C. Dong, J. Li and X. Han, *Chem. Eng. J.*, 2021, **408**, 127240.
- 15 Y. Guo, S. Ding, C. Shang, C. Zhang, M. Li, Q. Zhang, L. Gu, B. C. Heng, S. Zhang, F. Mei, Y. Huang, X. Zhang, M. Xu, J. Jiang, S. Guo, X. Deng and L. Chen, *Adv. Mater.*, 2024, **36**, 2306292.





- 16 Y. Cui, X. Chen, Y. Cheng, X. Lu, J. Meng, Z. Chen, M. Li, C. Lin, Y. Wang and J. Yang, *ACS Appl. Mater. Interfaces*, 2021, **13**, 22150–22158.
- 17 Y. Zhou, S. Fan, L. Feng, X. Huang and X. Chen, *Adv. Mater.*, 2021, **33**, 2104223.
- 18 Y. Liu, Z. Guo, F. Li, Y. Xiao, Y. Zhang, T. Bu, P. Jia, T. Zhe and L. Wang, *ACS Appl. Mater. Interfaces*, 2019, **11**, 31649–31660.
- 19 R. Li, S. Chen, X. Zhang, F. Zeng, X. Song, J. Yin and C. Jiang, *Sci. China Mater.*, 2024, **67**, 2985–2994.
- 20 L. Luo, W. Zhang, W. Su, J. Zhuo, L. Zhang, X. Xie, W. Zhang and J. Wang, *ACS Mater. Lett.*, 2024, **6**, 2487–2496.
- 21 R. Hu, Y. Fang, M. Huo, H. Yao, C. Wang, Y. Chen and R. Wu, *Biomaterials*, 2019, **206**, 101–114.
- 22 T. S. Mathis, K. Maleski, A. Goad, A. Sarycheva, M. Anayee, A. C. Foucher, K. Hantanasirisakul, C. E. Shuck, E. A. Stach and Y. Gogotsi, *ACS Nano*, 2021, **15**, 6420–6429.
- 23 M. Wen, S. Wang, R. Jiang, Y. Wang, Z. Wang, W. Yu, P. Geng, J. Xia, M. Li and Z. Chen, *Biomater. Sci.*, 2019, **7**, 4651–4660.
- 24 Y. Qian, C. Wang and Z.-G. Le, *Appl. Surf. Sci.*, 2011, **257**, 10758–10762.
- 25 S. T. Briskeby, M. Tsympkin, R. Tunold and S. Sunde, *RSC Adv.*, 2014, **4**, 44185–44192.
- 26 C. Li, G. Jiang, J. Yu, W. Ji, L. Liu, P. Zhang, J. Du, C. Zhan, J. Wang and B. Z. Tang, *Adv. Mater.*, 2023, **35**, 2208229.
- 27 X. Zheng, L. Wang, Y. Guan, Q. Pei, J. Jiang and Z. Xie, *Biomaterials*, 2020, **235**, 119792.
- 28 D. K. Roper, W. Ahn and M. Hoepfner, *J. Phys. Chem. C*, 2007, **111**, 3636–3641.
- 29 X. Deng, S. Liang, X. Cai, S. Huang, Z. Cheng, Y. Shi, M. Pang, P. Ma and J. Lin, *Nano Lett.*, 2019, **19**, 6772–6780.
- 30 Y. Liu, N. Nie, H. Tang, C. Zhang, K. Chen, W. Wang and J. Liu, *ACS Appl. Mater. Interfaces*, 2021, **13**, 11631–11645.
- 31 W. Li, B. Chen, H. Zhang, Y. Sun, J. Wang, J. Zhang and Y. Fu, *Biosens. Bioelectron.*, 2015, **66**, 251–258.
- 32 M. Huo, L. Wang, Y. Chen and J. Shi, *Nat. Commun.*, 2017, **8**, 357.
- 33 Y. Cheng, Y. Xia, Y. Sun, Y. Wang and X. Yin, *Adv. Mater.*, 2023, 2308033.
- 34 X. Zhou, Z. Wang, Y. K. Chan, Z. Jiao, Y. Yang, L. Li, J. Li, K. Liang and Y. Deng, *Adv. Funct. Mater.*, 2022, **32**, 2109469.
- 35 K. Aneesh, C. S. R. Vusa and S. Berchmans, *Sens. Actuators, B*, 2017, **253**, 723–730.
- 36 X. Bai, Z. Fu, X. Ma, Z. Zhang, J. Fan, E. Liu and J. Li, *J. Cleaner Prod.*, 2022, **369**, 133099.
- 37 Z. Xu, J. Jiang, Y. Li, T. Hu, J. Gu, P. Zhang, L. Fan, J. Xi, J. Han and R. Guo, *Small*, 2024, **20**, 2309096.
- 38 H. Yu, X. Xu, Z. Xie, X. Huang, L. Lin, Y. Jiao and H. Li, *ACS Appl. Mater. Interfaces*, 2022, **14**, 36947–36956.
- 39 Z. Yang, X. Fu, D. Ma, Y. Wang, L. Peng, J. Shi, J. Sun, X. Gan, Y. Deng and W. Yang, *Small*, 2021, **17**, 2103993.
- 40 Z. Lu, J. Gao, C. Fang, Y. Zhou, X. Li and G. Han, *Adv. Sci.*, 2020, **7**, 2001223.
- 41 Y. Maréchal, *J. Mol. Struct.*, 2011, **1004**, 146–155.
- 42 J.-B. Brubach, A. Mermet, A. Filabozzi, A. Gerschel and P. Roy, *J. Chem. Phys.*, 2005, **122**, 184509.
- 43 Y. Cui, C. Lin, M. Li, N. Zhu, J. Meng and J. Zhao, *J. Alloys Compd.*, 2022, **893**, 162181–162191.
- 44 T. Parker, D. Zhang, D. Bugallo, K. Shevchuk, M. Downes, G. Valurouthu, A. Inman, B. Chacon, T. Zhang, C. E. Shuck, Y.-J. Hu and Y. Gogotsi, *Chem. Mater.*, 2024, **36**, 8437–8446.
- 45 A. Karthika, P. Karuppasamy, S. Selvarajan, A. Suganthi and M. Rajarajan, *Ultrason. Sonochem.*, 2019, **55**, 196–206.
- 46 S. Niu, Z. Wang, M. Yu, M. Yu, L. Xiu, S. Wang, X. Wu and J. Qiu, *ACS Nano*, 2018, **12**, 3928–3937.
- 47 Y. Li, R. Fu, Z. Duan, C. Zhu and D. Fan, *ACS Nano*, 2022, **16**, 7486–7502.
- 48 H. Liu, Z. Hu, Q. Liu, P. Sun, Y. Wang, S. Chou, Z. Hu and Z. Zhang, *J. Mater. Chem. A*, 2020, **8**, 24710–24717.
- 49 C. Xing, S. Chen, X. Liang, Q. Liu, M. Qu, Q. Zou, J. Li, H. Tan, L. Liu, D. Fan and H. Zhang, *ACS Appl. Mater. Interfaces*, 2018, **10**, 27631–27643.
- 50 L.-S. Lin, T. Huang, J. Song, X.-Y. Ou, Z. Wang, H. Deng, R. Tian, Y. Liu, J.-F. Wang, Y. Liu, G. Yu, Z. Zhou, S. Wang, G. Niu, H.-H. Yang and X. Chen, *J. Am. Chem. Soc.*, 2019, **141**, 9937–9945.
- 51 S. M. AlShehri, J. Ahmed, T. Ahamad, P. Arunachalam, T. Ahmad and A. Khan, *RSC Adv.*, 2017, **7**, 45615–45623.
- 52 D. Zhang, M. Wang, W. Zhang and Q. Li, *Sens. Actuators, B*, 2020, **304**, 127234.
- 53 Y. Zhu, Z. Wang, R. Zhao, L. Feng, S. Gai and P. Yang, *ACS Nano*, 2022, **16**, 3105–3118.

